RSC Advances

PAPER

View Article Online
View Journal | View Issue

Cite this: *RSC Adv.*, 2025, **15**, 21311

First-principles investigations of electronic property modulation in the $FeCl_3/MoSi_2N_4$ heterojunction by strain, interlayer distance and vertical electric field variation†

Xinrui Chen, Su Su, Xuewen Wang, Xuanyu Chen, Syed Awais Ahmad, Lin Xu* and Weibin Zhang*

Received 7th April 2025
Accepted 16th June 2025

DOI: 10.1039/d5ra02387d

rsc.li/rsc-advances

This study investigated the changes in the electronic properties of the $FeCl_3/MoSi_2N_4$ heterostructure by modulating interlayer distance, in-plane strain, and external electric field. The results indicated that the $FeCl_3/MoSi_2N_4$ van der Waals heterostructure (vdWH) is an indirect band gap semiconductor with a band gap of 1.21/2.21 eV, as determined by a PBE/HSE06 calculations, and forms a type-I heterojunction. The equilibrium interlayer distance (ΔD) is 3.35 Å and altering it results in a decrease in the band gap. Subsequently, a biaxial strain (ε) was applied to the heterostructure. With compressive strain, the band gap shows a linear decrease. When $\varepsilon = -4\%$, the material changes from semiconductor to metallic state. Under tensile strains ranging from 1 to 3%, the band gap sharply decreases from 0.89 to 0.22 eV. Under a vertical external electric field in the −0.7 to 0.8 V $Å^{-1}$ range, the band gap stabilizes at around 0.9 eV. Notably, at −0.8 V $Å^{-1}$, the band gap reaches zero.

1. Introduction

Materials science is foundational in the modern industrial system, serving as the basis for all manufacturing activities and a critical driver of new technological revolutions.[1,2] Therefore, developing innovative materials is essential for enhancing the efficiency and quality of manufacturing processes. Geim and Novoselov prepared monolayer graphene through mechanical exfoliation,[3,4] igniting widespread interest in 2D material research. Graphene exhibits exceptional electrical conductivity, high absorption, superior carrier mobility,[5] good stability, and a large surface area. Despite numerous studies focusing on large-scale production and manufacturing techniques for graphene, practical applications remain limited.[6] This situation has prompted researchers to explore other 2D materials with semiconductor properties.[7]

Subsequently, various 2D materials exhibiting excellent performance have been discovered, including g-C_3N_4,[8] Janus MoSSe,[9] and TiO_2 (ref. 10 and 11) monolayers. They have shown significant progress in applications such as photocatalytic water splitting,[12] degradation of organic pollutants, environmental remediation,[13] and carbon dioxide reduction. Although 2D materials hold vast application potential in photocatalysis and optoelectronic devices, certain drawbacks still require optimization.

To overcome the limitations of 2D materials, van der Waals heterostructures (vdWH) demonstrate remarkable potential in modern electronics and optoelectronics, having ideal interface structure and efficient carrier separation and transport rates, flexible fabrication strategies, ultrafast bulk photovoltaic effects, and tunable band gaps.[14] Various heterojunctions, such as graphene/periodic porous graphene, MoS_2/WSe_2, MoS_2/TiO_2, graphene/hexagonal boron nitride, $CuInS_2/ZnS$,[15] and g-C_3N_4 S-scheme heterojunctions,[16] have been theoretically and experimentally studied. The successful construction of these heterojunctions indicates promising prospects for novel structures in optoelectronic devices.[17,18]

$MoSi_2N_4$ is a novel 2D-layered semiconductor material with unique electrical, optical, mechanical, and thermal properties. With a band gap of 1.74 eV, it falls into the category of indirect band gap semiconductors, which offer high transparency in the visible light range and demonstrate significant application potential in optoelectronics.[19] However, with the development of the semiconductor industry, the requirements for semiconductor materials for photoelectric devices have become increasingly high, and thus, the improvement of the electronic and optical properties of semiconductor materials has become a continued focus of research.

College of Physics and Electronics Information, Yunnan Key Laboratory of Opto-Electronic Information Technology, Key Laboratory of Advanced Technique & Preparation for Renewable Energy Materials-Ministry of Education, Yunnan Normal University, Kunming, 650500, P. R. China. E-mail: 220001@ynnu.edu.cn; xulin13888488199@163.com

† Electronic supplementary information (ESI) available. See DOI: https://doi.org/10.1039/d5ra02387d

The use of $FeCl_3$ as a dopant can regulate the microstructure and electronic properties of heterojunctions.[20] For example, few-layer graphene intercalated with $FeCl_3$ has been successfully prepared. In this heterojunction, the successful doping of $FeCl_3$ optimizes the electronic properties of the structure;[21,22] the $FeCl_3$ acts as a solid-state redox functional material doping both the graphene oxide (GO) and the single-wall carbon nanotube (SWCNT) film, resulting in a higher-conductivity composite film. As a result of doping with $FeCl_3$, the $FeCl_3$-GO/SWCNT/Si heterojunction achieves a higher conversion efficiency and good stability.[23]

Therefore, many researchers have found that constructing heterojunctions of $MoSi_2N_4$ with other 2D materials could enhance photocatalytic properties and offer possibilities in optoelectronic applications.[24,25] Research indicates that the $MoGe_2N_4$/$MoSi_2N_4$ heterolayer forms a type-II band alignment, effectively promoting the separation of electrons and holes while facilitating further movement of these charge carriers.[26] The $MoSi_2N_4$/GeC heterojunction possesses a stable structure, suitable band gap, strong redox potential, and high photogenerated carrier mobility. Applying strain or electric field can trigger a transition from a type-I to a type-II heterojunction,[27] thereby modifying its semiconductor properties. The $MoSi_2N_4$/WO_2 heterojunction demonstrates good kinetic stability and features a typical type-II band alignment. The $MoSi_2N_4$/WO_2 heterojunction efficiently improves the nanoelectronic and optoelectronic applications of monolayer $MoSi_2N_4$.[28] Tensile strain in the $MoSe_2$/$MoSi_2N_4$ heterojunction can enhance light absorption in the visible region, while compressive strain improves absorption in the ultraviolet region. Positive and negative electric fields can transform the system into a type-II heterojunction, allowing for the coexistence of type-II heterojunction characteristics alongside direct band properties. These discoveries provide valuable strategies for enhancing the performance of $MoSe_2$/$MoSi_2N_4$ heterojunctions in optoelectronic devices and expanding their application scope.[29] $MoSi_2N_4$/GaN represents a direct band gap type-I heterojunction, whereas $MoSi_2N_4$/ZnO constitutes an indirect band gap type-II heterojunction. By applying an external electric field or mechanical strain in the out-of-plane direction, the band structures of $MoSi_2N_4$/GaN and $MoSi_2N_4$/ZnO can undergo significant transformations, exhibiting rich transition behaviors, including shifts from type-I to type-II band alignments and transitions from direct to indirect band gaps. These findings reveal the tremendous design flexibility of $MoSi_2N_4$ for tunable composite materials for ultra-compact optoelectronic applications.[30]

This study describes the novel construction of the $FeCl_3$/$MoSi_2N_4$ vdWH by vertically stacking monolayer $FeCl_3$ on $MoSi_2N_4$. Based on first-principles calculations, we investigate the electronic structure of $FeCl_3$/$MoSi_2N_4$ vdWH and find that it exhibits type-I band alignment. To obtain superior characteristics in 2D materials, we systematically alter the interlayer distance, apply strain, and introduce external electric fields to modulate the electronic properties of the $FeCl_3$/$MoSi_2N_4$ vdWH. Our research reveals that the $FeCl_3$/$MoSi_2N_4$ vdWH possesses an indirect band gap of 1.21/2.21 eV, as given by the PBE/HSE06 calculations, and a work function of 6.08 eV, with a type-I band-edge alignment. Additionally, our findings reveal transitions between semiconductor and metal properties and type-I and type-II heterojunctions. We believe that the $FeCl_3$/$MoSi_2N_4$ vdWH will show promising application prospects in flexible electronic devices, optoelectronics, and photocatalytic applications.

2. Computational methods

This study employs first-principles calculations based on Density Functional Theory (DFT) to investigate the geometric optimization, electronic structure, and band alignment of the $FeCl_3$/$MoSi_2N_4$ vdWH. The calculations were performed using the Perdew–Burke–Ernzerhof (PBE) pseudopotential in the Vienna *Ab initio* Simulation Package (VASP), with the exchange–correlation potential optimized through the Generalized Gradient Approximation (GGA).[31,32] Recognizing the systematic band gap underestimation of the PBE-GGA functionals, we adopted the HSE06 hybrid functional (Heyd–Scuseria–Ernzerhof 2006) to achieve higher-precision band structure calculations.[33] The band gap data obtained using HSE06 have been included in the ESI.† At the same time, to visualize the discrepancy in band gap predictions arising from different computational algorithms, a comparative bar chart was constructed, as illustrated in Fig. S1.† Despite its tendency to underestimate absolute band gap values, the PBE functional demonstrates reliable accuracy in predicting band gap trends and elucidating underlying physical mechanisms. Notably, its computational efficiency surpasses that of HSE06, offering significant cost-effectiveness. For these combined reasons, PBE was selected for subsequent investigations of the heterostructure. For the monolayers of $FeCl_3$ and $MoSi_2N_4$ and the hybrid $FeCl_3$/$MoSi_2N_4$ vdWH, a cutoff energy of 450 eV was set for the electronic wave functions, along with a maximum of 100 self-consistent field repetitions. The K-point sampling in the Brillouin zone was configured to $6 \times 6 \times 1$, while the energy convergence criterion was defined as 10^{-8} eV. A vacuum layer thickness of 25 Å was introduced along the *Z*-axis to eliminate periodic boundary interactions. Considering the van der Waals interactions arising from weak interlayer coupling, Grimme's DFT-D3 method was employed for corrections.[34] During structural relaxation, the convergence thresholds for atomic energy and interatomic forces were established at 10^{-5} eV and 0.01 eV $Å^{-1}$, respectively. For subsequent electronic property calculations, to minimize the lattice mismatch, we constructed the $FeCl_3$/$MoSi_2N_4$ vdWH using a $1 \times 1 \times 1$ monolayer of $FeCl_3$ and a $2 \times 2 \times 1$ monolayer of $MoSi_2N_4$, resulting in a calculated lattice mismatch of 1.72%.

Our study employs a meticulously constructed $1 \times 1 \times 1$ $FeCl_3$/$2 \times 2 \times 1$ $MoSi_2N_4$ supercell to systematically investigate the electronic structure of the $FeCl_3$/$MoSi_2N_4$ vdWH and its responses to varying interlayer distances (ΔD), in-plane strains (ε), and applied electric fields (E). To preliminarily assess supercell-dependent band gap variations, we executed full structural relaxation of an additional $(2 \times 2 \times 1)$ $FeCl_3$/$(4 \times 4 \times 1)$ $MoSi_2N_4$ supercell configuration. The resultant band gap discrepancy of merely 0.03 eV and the band gaps are presented in Fig. S1.† Given that this minor discrepancy is substantially smaller than the regulatory scales studied later, and considering the prohibitive computational costs of high-precision DFT, we assert that the core physical mechanisms and

modulation trends revealed in the $(1 \times 1 \times 1)$ $FeCl_3/(2 \times 2 \times 1)$ $MoSi_2N_4$ supercell are representative within reasonable configuration limits. All subsequent calculations regarding interlayer spacing, biaxial strain, and vertical electric field effects were, therefore, performed exclusively on this supercell.

Initially, we explored the influence of interlayer distance on the electronic structure of the $FeCl_3/MoSi_2N_4$ vdWH, selecting an interlayer distance range from 1.5 to 6 Å. Subsequently, we applied in-plane strains ranging from −4 to 5% and external electric fields of −0.8 to 0.8 V $Å^{-1}$ to the $FeCl_3/MoSi_2N_4$ vdWH. Mechanical strains can be categorized into uniaxial and biaxial strains. The strain was calculated using the following formula:

$$\varepsilon = \frac{(L - L_0)}{L_0} \times 100\% \quad (1)$$

In eqn (1), L represents the lattice constant under strain, while L_0 denotes the lattice constant without strain. When $\varepsilon > 0$, it indicates tensile strain, whereas $\varepsilon < 0$ signifies compressive strain, with a variation magnitude of 1%. In subsequent calculations of the electronic structure of the $FeCl_3/MoSi_2N_4$ vdWH, we controlled the ΔD within the range of 2.95 to 5.00 Å, applied ε values ranging from −4 to 4%, and introduced E strengths from −0.8 to 0.8 V $Å^{-1}$.

The work functions of the $FeCl_3$ and $MoSi_2N_4$ monolayers, plus the $FeCl_3/MoSi_2N_4$ vdWH, define the energy barrier for electron emission from the Fermi level to vacuum. These values serve as intrinsic references for band alignment, formally expressed as:

$$\Phi = E_{vac} - E_F \quad (2)$$

We calculated the vacuum level and work function for the monolayer $FeCl_3$ using VASP, resulting in values of 1.86 eV and 6.23 eV, respectively. The vacuum level and work function of $MoSi_2N_4$ were determined to be 6.93 eV and 5.16 eV,[34] respectively, consistent with previous research. The vacuum level and work function of the $FeCl_3/MoSi_2N_4$ vdWH were found to be 7.67 eV and 6.08 eV, respectively. Using eqn (2), we calculated the Fermi levels of the monolayers: −4.37 eV for $FeCl_3$, 1.77 eV for $MoSi_2N_4$, and 1.59 eV for the $FeCl_3/MoSi_2N_4$ vdWH.

3. Results and discussion

3.1 Atomic geometries and stability of the $FeCl_3/MoSi_2N_4$ vdWH

To comprehensively study the $FeCl_3/MoSi_2N_4$ vdWH, we first optimized the geometric structures of the monolayers of $FeCl_3$ and $MoSi_2N_4$ and investigated their electronic properties. The

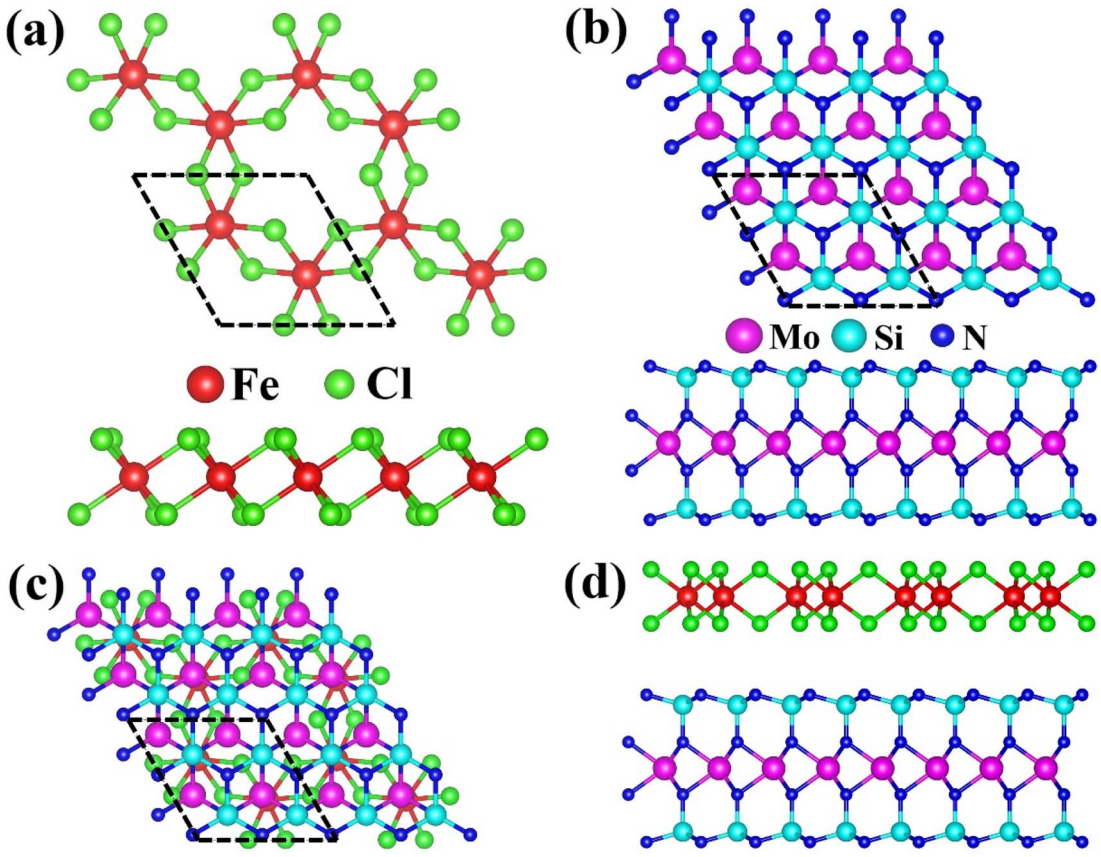

Fig. 1 (a) Top view and side view of the optimized atomic structure of the $FeCl_3$ monolayer. (b) Top view and side view of the optimized atomic structure of the $MoSi_2N_4$ monolayer. (c) Top view and (d) side view of the optimized atomic structure of the $FeCl_3/MoSi_2N_4$ vdWH. Magenta, cyan, blue, red, and green balls represent molybdenum, silicon, nitrogen iron and chlorine atoms.

top and side views of the atomic structure of the 2D monolayer $FeCl_3$ are shown in Fig. 1(a). Each unit cell of the $FeCl_3$ monolayer contains eight atoms, comprising two Fe atoms and six Cl atoms, with covalent bonds formed between them. After geometric optimization, the calculated lattice parameters for the $1 \times 1 \times 1$ $FeCl_3$ unit cell were found to be $a = b = 5.91$ Å, and the Fe–Cl bond length was measured to be 2.27 Å. For the $1 \times 1 \times 1$ $MoSi_2N_4$ unit cell, the calculated lattice parameters were $a = b = 2.90$ Å,[35] which aligns with previously reported values. Due to the differing lattice parameters between the $FeCl_3$ and $MoSi_2N_4$ monolayers, the construction of a supercell was required. To successfully create this supercell, we utilized a $2 \times 2 \times 1$ $MoSi_2N_4$ unit cell; the corresponding top and side views of the atomic structure are displayed in Fig. 1(b). Each unit cell of $MoSi_2N_4$ contains twenty-eight atoms, including four Mo atoms, eight Si atoms, and sixteen N atoms, with covalent bonds formed among them. Following geometric optimization, the calculated lattice parameters for $MoSi_2N_4$ were determined to be $a = b = 5.81$ Å. The Mo–N bond length was measured to be 2.09 Å, the N–Si bond length was 1.75 Å, and the Si–Mo bond length was 3.43 Å, all of which are consistent with data from other reports.

The top view of the atomic structure of the $FeCl_3/MoSi_2N_4$ vdWH is presented in Fig. 1(c), while the side view is shown in Fig. 1(d). Each unit cell of the $FeCl_3/MoSi_2N_4$ vdWH contains thirty-six atoms, consisting of two Fe atoms, six Cl atoms, four Mo atoms, eight Si atoms, and sixteen N atoms, with covalent bonds formed within the layers. As illustrated in Fig. 1(d), no covalent bonds are formed between the layers; rather, these surface layers are stacked through weak van der Waals forces. After geometric optimization, the calculated lattice parameters for the $FeCl_3/MoSi_2N_4$ vdWH were found to be $a = b = 5.91$ Å. The Fe–Cl bond length was measured to be 2.27 Å, the Mo–Si bond length was 3.43 Å, the Mo–Fe bond length was 8.32 Å, the Mo–N bond length was 2.10 Å, and the N–Si bond length was 1.77 Å.

Moreover, recognizing that stacking configurations critically govern material stability, we designed four distinct heterostructures through lateral displacement of the $FeCl_3$ monolayer relative to a fixed $MoSi_2N_4$ monolayer. As shown in Fig. 2(a), this stacking structure deliberately avoided atomic registry engineering, maintaining the naturally formed stacking architecture, as described above. This unmodified stacking arrangement preserves the intrinsic interlayer charge transfer characteristics governed by van der Waals interactions. The other stacking configurations featured vertical alignment between Fe and Mo atoms (Fig. 2(b)), between Cl and N atoms (Fig. 2(c)), or between Fe and Si atoms (Fig. 2(d)). All four structures underwent comprehensive structural relaxation to achieve fully optimized atomic positions and lattice parameters.

To evaluate the stability of these heterostructures, we calculated the binding energy (E_b) for the four stacking structures. Our systematic DFT computations demonstrate that the four distinct stacking configurations exhibit binding energies of −5.81, −5.38, −5.74 and −5.77 eV, accompanied by corresponding band gap values of 0.93, 0.94, 0.93, and 0.96 eV, respectively. Collectively demonstrating robust stability, all structures show nearly identical band gaps, which indicates that the stacking structures have a negligible effect on the band gap across configurations. However, the binding energy of structure A is measurably lower than those of structures B1–B3, establishing it as the most stable structure. The calculation formulas for binding energy and cohesive energy are as follows:[40]

$$E_b = E_T - E_{MSN} - E_{FC} \quad (3)$$

where E_T represents the total energy of the $MoSi_2N_4/FeCl_3$ vdWH, and E_{MSN} and E_{FC} represent the total energies of the $MoSi_2N_4$ monolayer and the $FeCl_3$ monolayer, respectively.

Dynamic stability was verified *via* phonon dispersion calculations across the entire Brillouin zone, as illustrated in

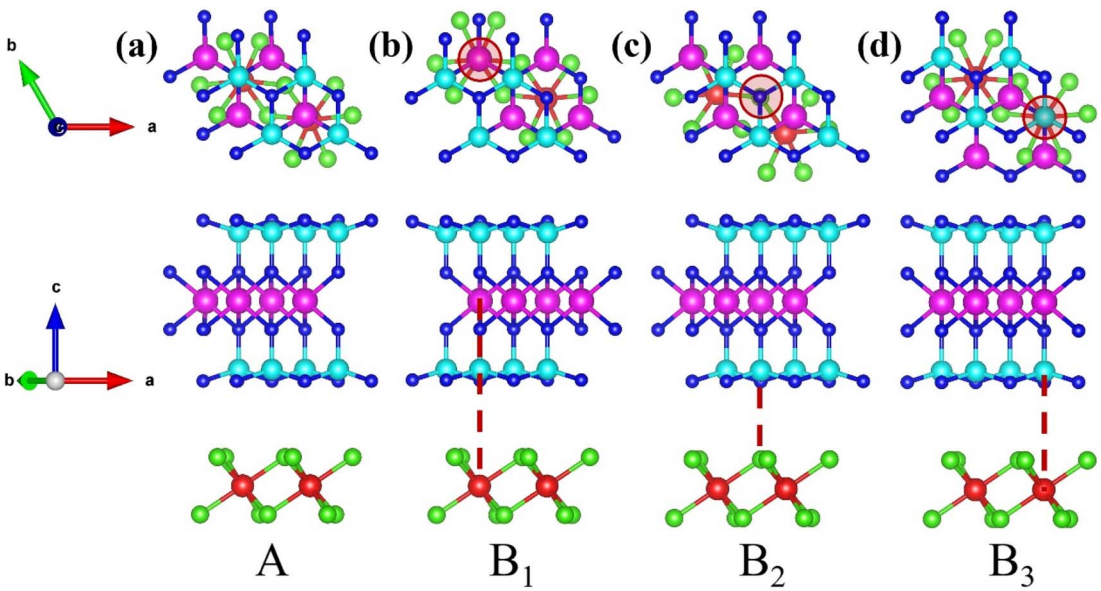

Fig. 2 Top view and side view of the optimized $FeCl_3/MoSi_2N_4$ vdWH: (a) A stacking, (b) B_1 stacking, (c) B_2 stacking, and (d) B_3 stacking.

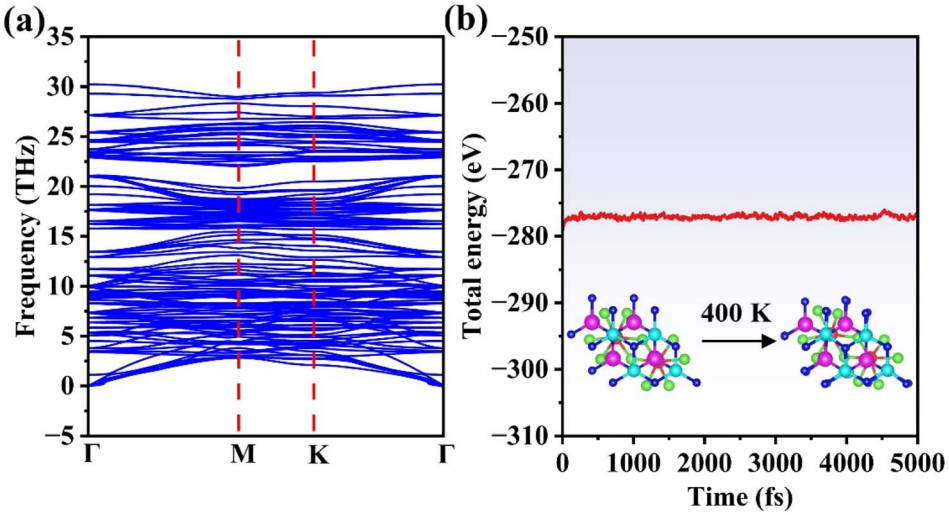

Fig. 3 (a) Phonon spectrum of the A stacking structure and (b) evolution of the total energy of the A stacking structure during AIMD simulations at 400 K. The inset in (b) shows the atomic structure of the A stacking configuration at the end of the AIMD simulation.

Fig. 3(a). The absence of imaginary frequencies in all phonon branches confirms the dynamic stability of the $FeCl_3/MoSi_2N_4$ vdWH.

Additionally, our assessment of the thermal stability in the A stacking configuration at 400 K, conducted *via* atomic-scale molecular dynamics (AIMD) simulations (Fig. 3(b)), employed a 4000 fs trajectory with 1 fs time steps. The AIMD results reveal no evidence of structural degradation in the $FeCl_3/MoSi_2N_4$ vdWH at this temperature, confirming its robust thermal stability under ambient conditions. Consequently, the A stacking configuration maintains exceptional structural integrity. Based on these findings, we selected this architecture for subsequent investigations.

3.2 Electronic structure of the $FeCl_3/MoSi_2N_4$ vdWH

We then calculated the band structures for the $FeCl_3$ monolayer, $MoSi_2N_4$ monolayer, and $FeCl_3/MoSi_2N_4$ vdWH. Fig. 4(a) displays the band structure of monolayer $FeCl_3$, in which the conduction band minimum (CBM) is located at the M-point, and the valence band maximum (VBM) is also situated at the M-point in the Brillouin zone. The CBM and VBM coincide, which indicates that $FeCl_3$ is a direct band gap semiconductor with a band gap of 1.21/2.75 eV.

Fig. 4(b) illustrates the band structure of $MoSi_2N_4$. The CBM is located at the K-point, while the VBM is at the Γ point. As the CBM and VBM do not occupy the same point in the Brillouin zone, $MoSi_2N_4$ is an indirect band gap semiconductor with a band gap of 1.79/2.35 eV,[35] consistent with previous reports. Additionally, the Fermi level of $MoSi_2N_4$ is close to the VBM, indicating a relatively high concentration of holes and fewer electrons in the conduction band. Hence, holes are the primary charge carriers in the conductivity process, confirming that $MoSi_2N_4$ is a p-type semiconductor.

Fig. 4(c) presents the $FeCl_3/MoSi_2N_4$ vdWH band structure, in which the CBM is positioned at the K-point in the Brillouin zone and the VBM at the M-point. Upon the formation of a heterojunction between $FeCl_3$ and $MoSi_2N_4$, electrons transfer from the conduction band of $MoSi_2N_4$ to the conduction band of $FeCl_3$, while the holes migrate from the valence band of $MoSi_2N_4$ to the valence band of $FeCl_3$. Consequently, the CBM of $FeCl_3$ dominates the conduction band alignment of the heterojunction due to its lower energy level, while the VBM of $FeCl_3$ governs the valence band alignment, owing to its higher energy level. Crucially, electron transitions still require overcoming the momentum mismatch between the M-point and K-point in the Brillouin zone, indicating that the $FeCl_3/MoSi_2N_4$ vdWH is an indirect band gap semiconductor with a band gap of 1.21/2.21 eV, which is smaller than that of $MoSi_2N_4$, suggesting improved electronic properties. The Fermi level penetrating into the valence band signifies a degenerate semiconductor state at the interface, exhibiting quasi-metallic conductivity. The underlying mechanism arises from strong interfacial coupling, inducing substantial charge redistribution. This charge transfer generates exceptionally high effective hole concentrations, leading to heavy doping degeneracy in the localized interfacial region. Under degenerate conditions, the dense hole population partially fills the VBM, pinning the Fermi level within the valence band. These partially filled states confer metal-like high conductivity, while fundamentally retaining a semiconducting character—distinct from conventional metals with fully overlapping bands.

Furthermore, based on the projected band structure of the $FeCl_3/MoSi_2N_4$ vdWH shown in Fig. 4(d), we find that the monolayer $FeCl_3$ primarily contributes the VBM and CBM. Thus, the $FeCl_3/MoSi_2N_4$ vdWH exhibits a type-I band alignment, which hinders the separation of electrons and holes and suppresses their transport within the heterostructure. However, this alignment is characterized by high carrier recombination efficiency, indicating that photogenerated electrons and holes are confined within the same region. This overlap of electrons

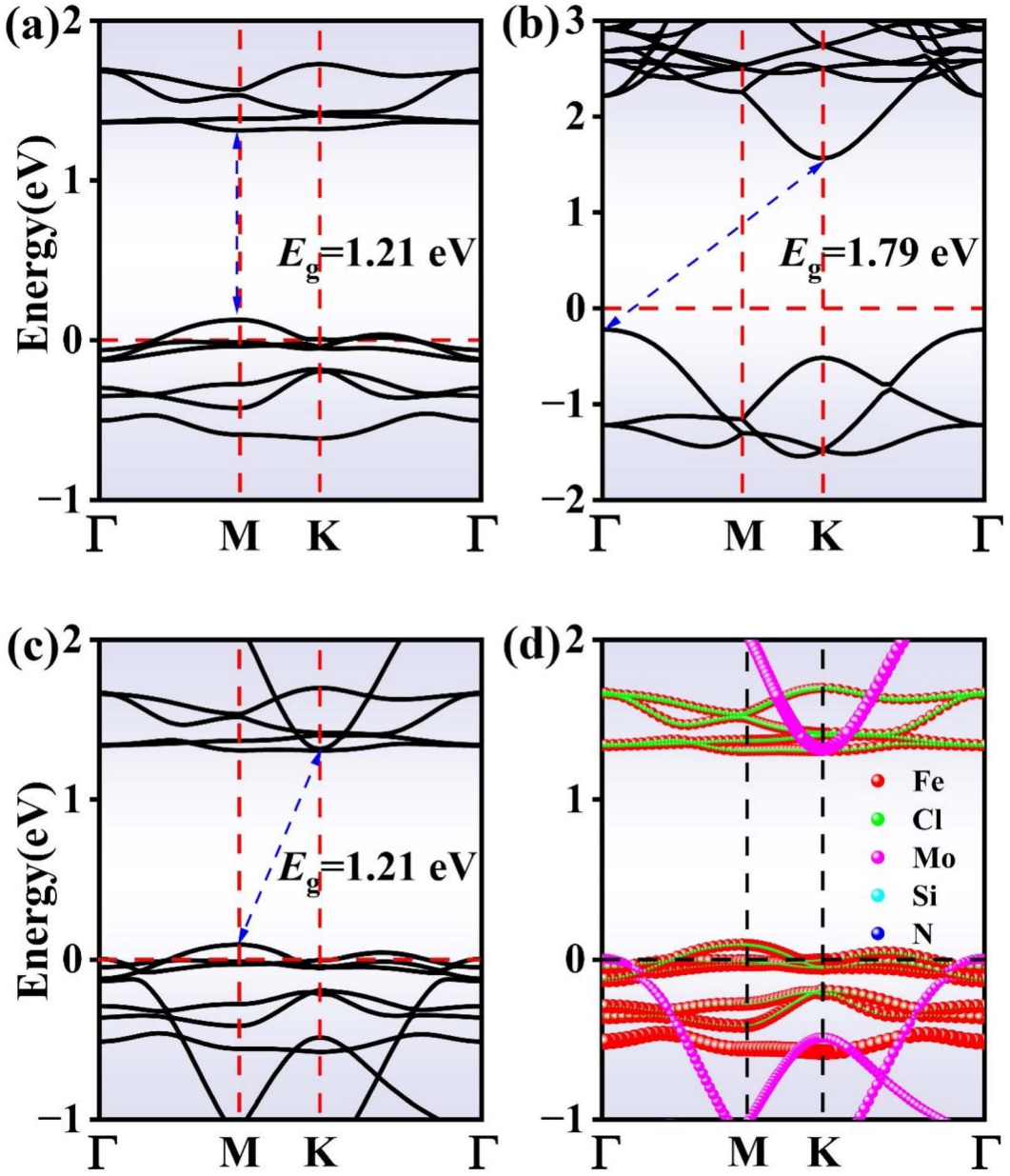

Fig. 4 Band structure of state for the (a) $FeCl_3$ monolayer, (b) $MoSi_2N_4$ monolayer and (c) $FeCl_3/MoSi_2N_4$ vdWH. (d) Weighted band structure of the $FeCl_3/MoSi_2N_4$ vdWH. The Fermi level is set to zero.

and holes facilitates radiative recombination and is advantageous for light-emitting applications.[36]

The reduced band gap in the $FeCl_3/MoSi_2N_4$ vdWH compared with that of monolayer $MoSi_2N_4$ implies a broader optical absorption spectrum. A comparative optical absorption analysis is detailed in the ESI, as illustrated in Fig. S4.†

In addition to studying the band structure, we investigated the total density of states (DOS) and the partial density of states (PDOS) for the $FeCl_3$ monolayer, $MoSi_2N_4$ monolayer, and $FeCl_3/MoSi_2N_4$ vdWH. Fig. 5(a) shows the total DOS and PDOS of the $FeCl_3$ monolayer. Within the energy range of −1 to 0 eV, the valence band edge (VBE) is primarily derived from the contributions of the Fe 3d states. In the energy range of 0 to 2 eV, the conduction band edge (CBE) is also mainly sourced from the contributions of the Fe 3d states. Overall, the bands near the Fermi level are predominantly contributed by the Fe 3d orbitals, while the contributions from the Cl 3p orbitals are relatively minor.

Fig. 5(b) depicts the total DOS and PDOS of the $MoSi_2N_4$ monolayer. In the energy range of −2 to 0 eV, the VBE is mainly attributed to contributions from the Mo 4d states. In the energy range of 0 to 3 eV, the CBE is likewise primarily derived from the Mo 4d states. Thus, the bands near the Fermi level in this material are predominantly influenced by the Mo 4d orbitals, whereas the contributions from the Si 3p and N 2p orbitals are comparatively small.

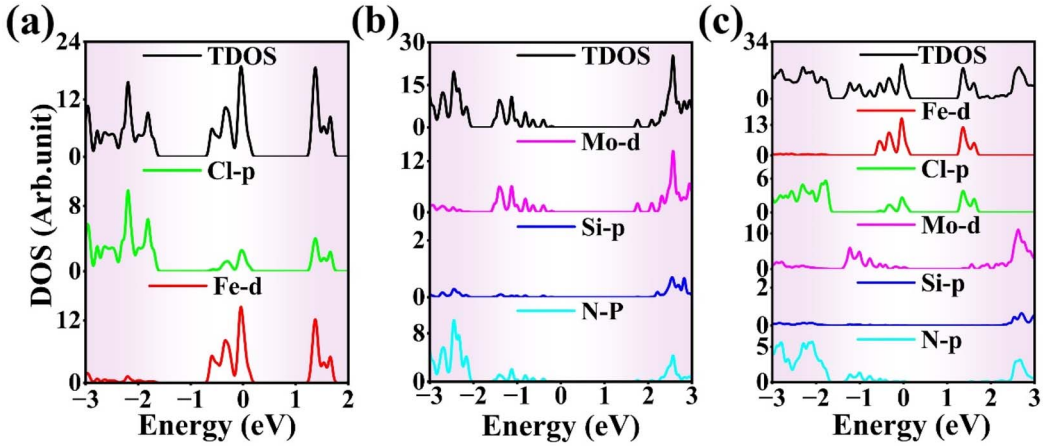

Fig. 5 DOS of the (a) $FeCl_3$ monolayer, (b) $MoSi_2N_4$ monolayer and (c) $FeCl_3/MoSi_2N_4$ vdWH. The Fermi level is set to zero.

Fig. 5(c) illustrates the total DOS and PDOS of the $FeCl_3/MoSi_2N_4$ vdWH. Within the energy range of −1 to 0 eV, the VBE is primarily sourced from the Fe 3d states. In the energy range of 0 to 2 eV, the CBE results mainly from the hybridization between the Fe 3d and Cl 3p orbitals, with no contribution from $MoSi_2N_4$ at the band edges. The Fe 3d orbitals chiefly contribute the bands near the Fermi level, while contributions from the Cl 3p, Mo 4d, Si 3p, and N 2p orbitals are minimal.

Following the establishment of the band structure and DOS distribution of the material, subsequent analysis of carrier concentration was critical. First, electrons inherently conform to the Fermi–Dirac distribution statistics as fermionic particles:

$$f(E) = \frac{1}{1 + \exp\left(\frac{E - E_F}{K_0 T}\right)} \quad (4)$$

At room temperature (T = 300 K), where k_0 denotes the Boltzmann constant, the net carrier concentration in a semiconductor is defined as the sum of electron and hole concentrations: $n_{net} = n + p$, with E_F representing the Fermi energy at this specific temperature. At thermal equilibrium, the equilibrium electron concentration in the conduction band, denoted as n_0, and the equilibrium hole concentration in the valence band, denoted as p_0, are governed by the following expressions.

$$n_0 = \frac{1}{V}\int_{E_c}^{E_c'} f(E) g_c(E) \mathrm{d}E \quad (5)$$

$$p_0 = \frac{1}{V}\int_{E_v'}^{E_v} [1 - f(E)] g_v(E) \mathrm{d}E \quad (6)$$

where V represents the volume of the supercell, while E_c', E_C, E_V, and E_v' denote the energy levels at the conduction band maximum, CBM, VBM, and valence band minimum, respectively. The functions $g_c(E)$ and $g_v(E)$ correspond to the DOS in the vicinity of the CBE and VBE.

In this way, we obtained the carrier densities from the calculated electronic structures. Through rigorous computational analysis, we determined that the heterostructure exhibits a net carrier concentration of 5.15×10^{14} cm^{-2}, with hole and electron concentrations quantified as 4.46×10^{14} and 6.87×10^{13} cm^{-2}, respectively. The Fermi level being located within the valence band signifies the onset of a degenerate regime in the semiconductor, where the hole concentration becomes overwhelmingly dominant (10 times greater than the electron concentration). This behavior aligns with characteristic features of heavily doped p-type semiconductors.

3.3 Work functions of the $FeCl_3/MoSi_2N_4$ vdWH

The work function (Φ) corresponds to the minimum energy barrier for electron emission from the Fermi energy to the vacuum level. When constructing a vdWH from two different materials, electrons will flow from the material with a smaller work function to the one with a larger work function, thereby aligning their Fermi levels.[37,38] To analyze the charge distribution in the $FeCl_3/MoSi_2N_4$ vdWH, we obtained the work functions of the $FeCl_3$ monolayer, $MoSi_2N_4$ monolayer, and $FeCl_3/MoSi_2N_4$ vdWH, as shown in Fig. 6(a)–(c). The work function of the $FeCl_3$ monolayer is 6.23 eV, which is higher than that of the $MoSi_2N_4$ monolayer at 5.16 eV. The work function of the $FeCl_3/MoSi_2N_4$ vdWH is 6.08 eV, positioned between those of the $FeCl_3$ and $MoSi_2N_4$ monolayers.

As the $FeCl_3$ monolayer has a greater work function than the $MoSi_2N_4$ monolayer, when the $FeCl_3/MoSi_2N_4$ vdWH is formed, electrons diffuse from the $MoSi_2N_4$ monolayer to the $FeCl_3$ monolayer. This results in a significant number of holes being left behind in the $MoSi_2N_4$ monolayer, while a large number of electrons accumulate in the $FeCl_3$ monolayer. Consequently, the Fermi level of the $FeCl_3$ monolayer experiences a negative shift of 0.15 eV, while that of the $MoSi_2N_4$ monolayer shifts positively by 0.92 eV, until both Fermi levels align at the same position. Using the vacuum level (E_{vac}) as the energy reference (0 points), we determined the $FeCl_3/MoSi_2N_4$ vdWH band alignment. As illustrated in Fig. 6(d), we compared the position for the $FeCl_3/MoSi_2N_4$ vdWH with those of the isolated $FeCl_3$ and $MoSi_2N_4$ monolayers.

The $FeCl_3/MoSi_2N_4$ vdWH exhibits a type-I band alignment, which is consistent with the above DOS, indicating that

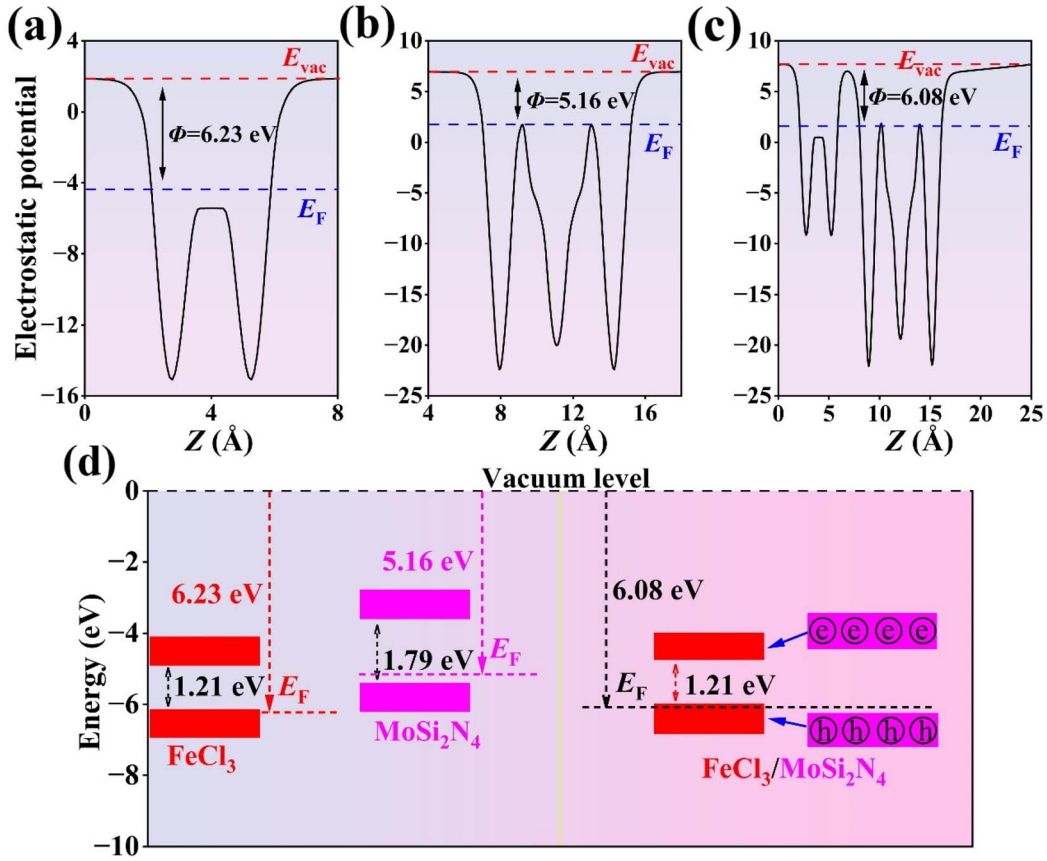

Fig. 6 Electrostatic potential curves of the (a) $FeCl_3$ monolayer, (b) $MoSi_2N_4$ monolayer and (c) $FeCl_3/MoSi_2N_4$ vdWH along the *Z* direction. The Fermi level and vacuum level are denoted by the long blue and red dashed lines, respectively. (d) Band alignment of $FeCl_3/MoSi_2N_4$ vdWH before and after forming the contact.

electrons and holes are confined within the same layer. In the $FeCl_3/MoSi_2N_4$ type-I heterojunction structure, as both the CBM and VBM originate from the $FeCl_3$ monolayer, there is no need for electrons to transfer to the $MoSi_2N_4$ monolayer during electronic transitions. This implies that both electrons and holes can migrate from the $MoSi_2N_4$ monolayer to the $FeCl_3$ monolayer, facilitating the formation of electron–hole pairs. Furthermore, this indicates that the $FeCl_3/MoSi_2N_4$ vdWH possesses excellent electron transport properties, suggesting high photoelectric conversion efficiency, making it suitable for applications in optoelectronic devices, such as light-emitting diodes and lasers.

3.4 Charge density difference of the $FeCl_3/MoSi_2N_4$ vdWH

Additionally, to further analyze the charge distribution in the $FeCl_3/MoSi_2N_4$ vdWH, we calculated the charge density difference. Fig. 7(a) displays the plane-averaged charge density difference of the $FeCl_3/MoSi_2N_4$ vdWH, illustrating variations in charge density along the *Z* direction. Positive values (yellow regions) indicate electron accumulation, while negative values (cyan regions) represent electron depletion. As depicted in Fig. 7(b), the formation of regions with electron accumulation (yellow areas) and depletion (cyan areas) signifies that the $FeCl_3/MoSi_2N_4$ vdWH undergoes charge redistribution to achieve interfacial charge balance.

Significantly, the top layer of the $FeCl_3$ monolayer has a prominent yellow region, indicating electron accumulation, while the lower part of the $MoSi_2N_4$ monolayer mostly exhibits cyan, signifying electron depletion. Consequently, electrons mostly migrate from the $MoSi_2N_4$ monolayer to the $FeCl_3$ monolayer, consistent with the band alignment findings shown in Fig. 6(d).

Moreover, charge redistribution mostly occurs between the $FeCl_3$ monolayer and the $FeCl_3/MoSi_2N_4$ vdWH, while the changes in electronic charge inside the $MoSi_2N_4$ monolayer are negligible. This phenomenon is caused by the weak van der Waals interactions between the $FeCl_3$ and $MoSi_2N_4$ monolayers, which enable the localization or redistribution of charges at the interface.

3.5 Tuning the electronic structure through interlayer distance

To determine the influence of interlayer distance on the band gap and structure of the $FeCl_3/MoSi_2N_4$ vdWH, we fixed the $MoSi_2N_4$ monolayer and vertically adjusted the position of the $FeCl_3$ monolayer to modify the heterojunction distance, as depicted in Fig. 8(a). Experimentally, the interlayer distance in

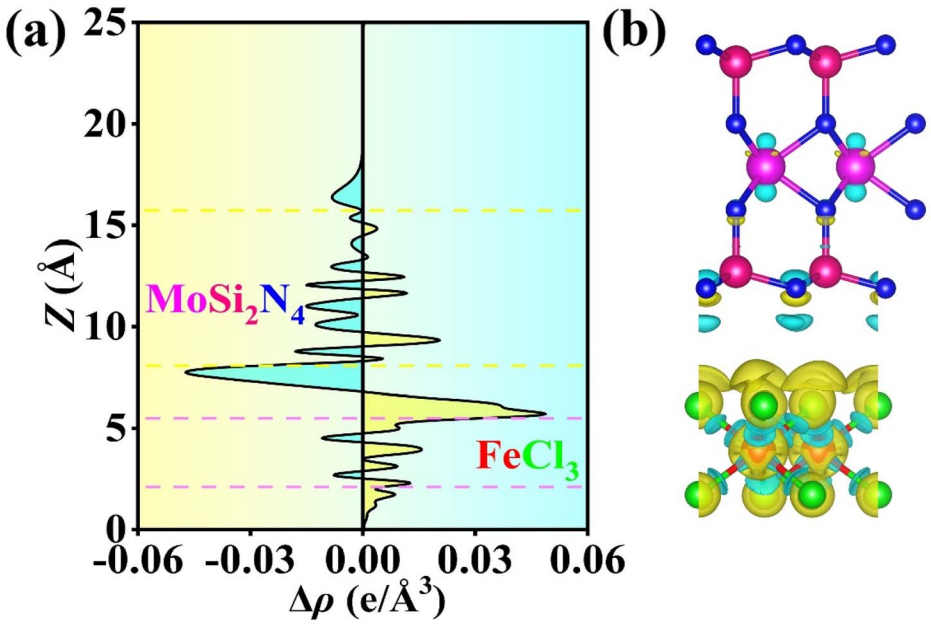

Fig. 7 (a) Plane-averaged and (b) three-dimensional charge density differences of $FeCl_3/MoSi_2N_4$ vdWH. Red, green, magenta, pink and blue balls represent the iron, chlorine, molybdenum, silicon, and nitrogen atoms, respectively.

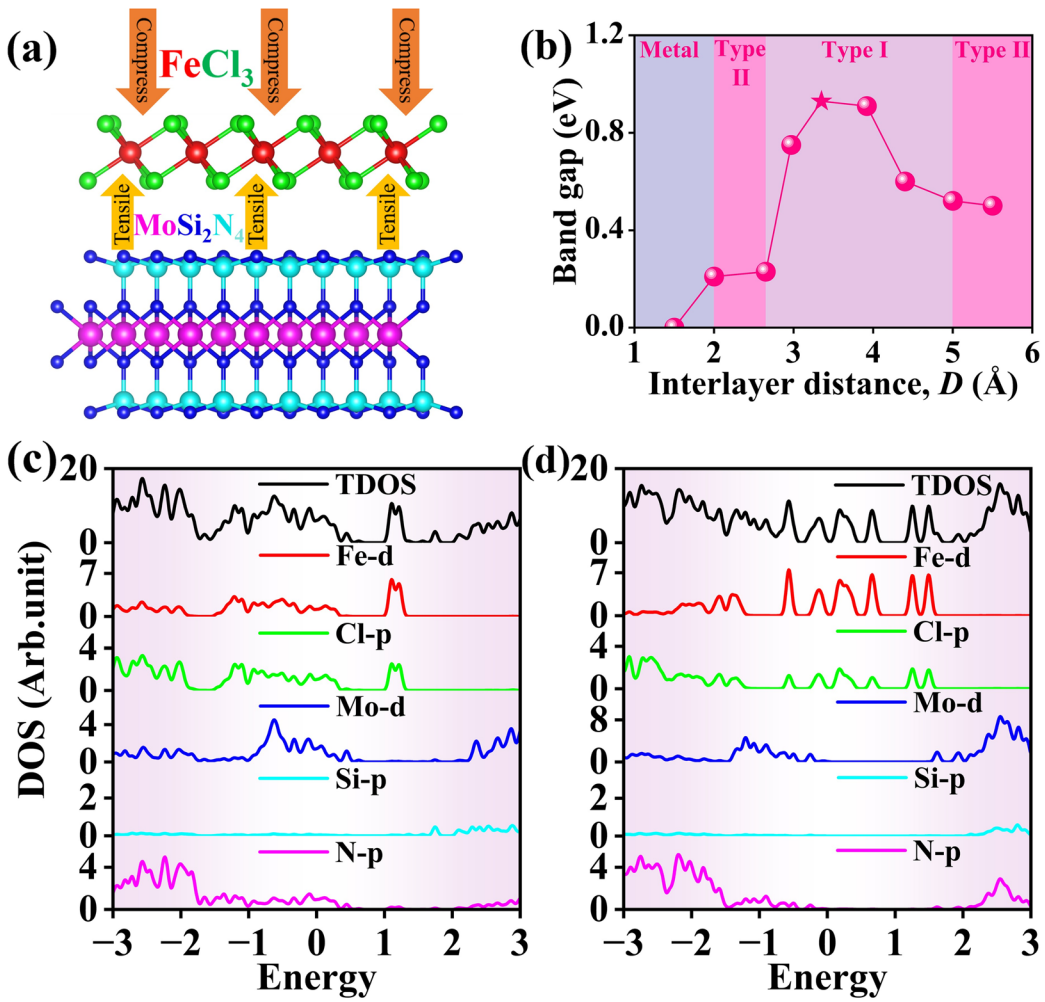

Fig. 8 (a) Schematic model of applied strain along the *z* direction. (b) Change in the band gap of the $FeCl_3/MoSi_2N_4$ vdWH as a function of interlayer coupling with changing the interlayer distance. DOS of $FeCl_3/MoSi_2N_4$ vdWH for interlayer distances of (c) 2.00 and (d) 2.65 Å .

2D-material-based heterostructures can be controlled by applying pressure using the tip of a scanning tunneling microscope.[39] The relationship between the band gap of the $FeCl_3/MoSi_2N_4$ vdWH and the interlayer distance is illustrated in Fig. 8(b).

Initially, the equilibrium interlayer distance, which is represented as ΔD, was 3.35 Å. When ΔD was increased from 3.35 to 5.00 Å, the band gap decreased from 0.93 to 0.52 eV. Subsequently, when ΔD reached 6 Å, the band gap stabilized at 0.50 eV. Conversely, when ΔD was decreased from 3.35 to 2.00 Å, the band gap experienced a significant drop from 0.93 to 0.21 eV. Finally, reducing ΔD further from 2.00 to 1.50 Å resulted in the band gap diminishing to 0 eV. When the interlayer spacing of the heterojunction changes, the strength of the van der Waals forces also changes, leading to alterations in the interlayer interactions within the heterojunction, which in turn affects the variation in the band gap. The significance of this finding lies in revealing the nonlinear relationship between band gap evolution and interlayer distance variation. Notably, when the interlayer distance change exceeds 4.5 Å, the rate of band gap reduction slows significantly. With increasing overlap, the band gap diminishes, eventually reaching zero, indicating that the $FeCl_3/MoSi_2N_4$ vdWH transitions from a semiconductor to a metal.

Fig. 8(c) shows the DOS at $\Delta D = 2.00$ Å. From the figure, it can be observed that the VBE is provided by the Mo 4d orbitals in the $MoSi_2N_4$ monolayer, while the CBE is contributed by the Fe 3d orbitals in the $FeCl_3$ monolayer. Therefore, the $FeCl_3/MoSi_2N_4$ vdWH exhibits a type-II band alignment. Fig. 8(d) presents the DOS at $\Delta D = 2.65$ Å; it can be seen that both the VBE and CBE are provided by the Fe 3d orbitals in the $FeCl_3$ monolayer, indicating a type-I band alignment. Similarly, using differential DOS plots, we conclude that the $FeCl_3/MoSi_2N_4$ vdWH displays type-II band alignment at $\Delta D = 2.00$, 5.00, and 5.50 Å. In contrast, the $FeCl_3/MoSi_2N_4$ vdWH exhibits type-I band alignment at $\Delta D = 2.95$, 3.35, 3.92, and 4.40 Å.

3.6 Effects of tension and compression on electronic structure

Applied strain may significantly modify the band structure of the $FeCl_3/MoSi_2N_4$ vdWH. This approach enhances basic scientific research in semiconductor technologies and promotes numerous practical applications in daily life, covering multiple fields from electronic devices to innovative energy solutions. These technical developments improve device efficiency and effectiveness, providing simplicity and innovation in our lives.

Mechanical strain encompasses both biaxial and uniaxial strain,[40] with this work primarily focusing on biaxial strain. We chose to focus on biaxial strain for three reasons: (i) theoretical perspective: biaxial strain preserves the in-plane symmetry of the system, avoiding anisotropic band renormalization induced

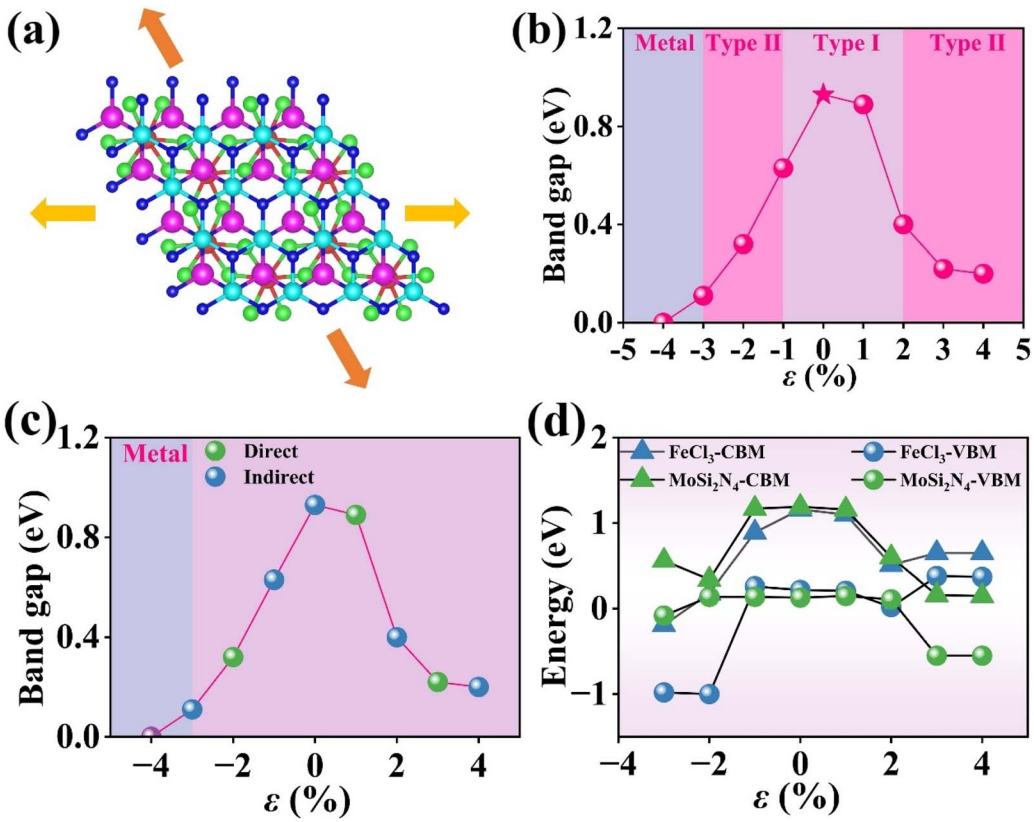

Fig. 9 (a) Schematic model of applied in-plane strain. (b) Variation of the band gap of $FeCl_3/MoSi_2N_4$ vdWH as a function of in-plane strain. (c) Nature of the band gap and (d) shifts in band-edge alignment under applied strain for the $FeCl_3/MoSi_2N_4$ vdWH.

by uniaxial strain. (ii) Experimental feasibility: uniform in-plane strain within heterostructures can be effectively achieved through biaxial pre-stretching techniques using flexible substrates, which is a well-established methodology in strain engineering practices. (iii) Heterostructure compatibility: the uniform and symmetric nature of biaxial strain enables coordinated interlayer deformation within heterostructures. In contrast, uniaxial strain introduces directional constraints that frequently lead to interlayer misalignment and subsequent failure in strain transfer, particularly in van der Waals heterostructures.

Fig. 9(a) illustrates the direction and angle of the applied strain on the $FeCl_3/MoSi_2N_4$ vdWH, with the orientations being horizontal and diagonally downward and upward at a 60° angle to the vertical.

Fig. 9(b) illustrates the correlation between the applied strain and the band gap. In this study, we calculated the variation of the band gap of the $FeCl_3/MoSi_2N_4$ vdWH under biaxial strain ranging from −4 to 4%. When the strain is increased from 0 to 4%, the band gap significantly decreases from 0.93 to 0.20 eV. Conversely, when the strain is decreased from zero to −3%, the band gap exhibits a nearly linear decline, dropping from 0.93 to 0.11 eV. However, as the strain decreases from −3 to −4%, the band gap reaches zero. This phenomenon is due to lattice distortion caused by the applied strain, leading to band bending that causes the CBM and VBM to move closer together, or even overlap, resulting in a band gap of zero. The transition of the $FeCl_3/MoSi_2N_4$ vdWH to a band gap of zero marks its transformation from a semiconductor to a metal. Based on the DOS results, the $FeCl_3/MoSi_2N_4$ vdWH changes from type-I to type-II heterojunction at $\varepsilon = -3$, −2, 2, 3 and 4%, as illustrated in Fig. 9(b).

Fig. 9(c) demonstrates the reversible indirect-to-direct band gap evolution in the heterostructure under biaxial strain. Under conditions of zero strain, as well as at −3, −1, 2 and 4% applied strain, electrons transfer from the higher energy state in the conduction band to the CBM, while holes migrate from the lower energy state in the valence band to the VBM, as the CBM and VBM reside at different points in the Brillouin zone. Moreover, electron transitions require overcoming the momentum mismatch between the M-point and K-point in the Brillouin zone, which indicates that the $FeCl_3/MoSi_2N_4$ vdWH is an indirect band gap semiconductor. In contrast, under conditions of −2, 1 and 3% applied strain, the VBM and VBM coincide at the same high-symmetry point in the Brillouin zone, enabling direct electron transitions without requiring phonon assistance, which indicates that the $FeCl_3/MoSi_2N_4$ vdWH is a direct band gap semiconductor.

To elucidate the strain-induced band gap modulation mechanism, we analyzed the band-edge evolution in the $FeCl_3/MoSi_2N_4$ vdWH under biaxial deformation. These strain responses are graphically represented in Fig. 9(d). Within the −1 to +1% biaxial strain range, the heterostructure undergoes elastic lattice deformation, in which the band edges of $FeCl_3$ and $MoSi_2N_4$ exhibit quasi-rigid shifting, resulting in minimal band gap variation. Beyond the critical ± 1% strain threshold, inelastic lattice distortion occurs, triggering significant bond-angle distortions and interlayer coupling reconstruction. This induces asynchronous and pronounced shifts in the band edges of both materials, ultimately leading to substantial band gap modifications.

Fig. 10(a) shows the DOS at $\varepsilon = -2\%$. It can be observed that the VBE is provided by the Mo 4d orbitals in the $MoSi_2N_4$ monolayer, while the Fe 3d orbitals in the $FeCl_3$ monolayer contribute to the CBE. Thus, the $FeCl_3/MoSi_2N_4$ vdWH exhibits a type-II band alignment. Fig. 10(b) depicts the DOS at $\varepsilon = 0$, in which both the valence and conduction band edges are provided by the Fe 3d orbitals in the $FeCl_3$ monolayer, indicating that the $FeCl_3/MoSi_2N_4$ vdWH has a type-I band alignment at this strain level.

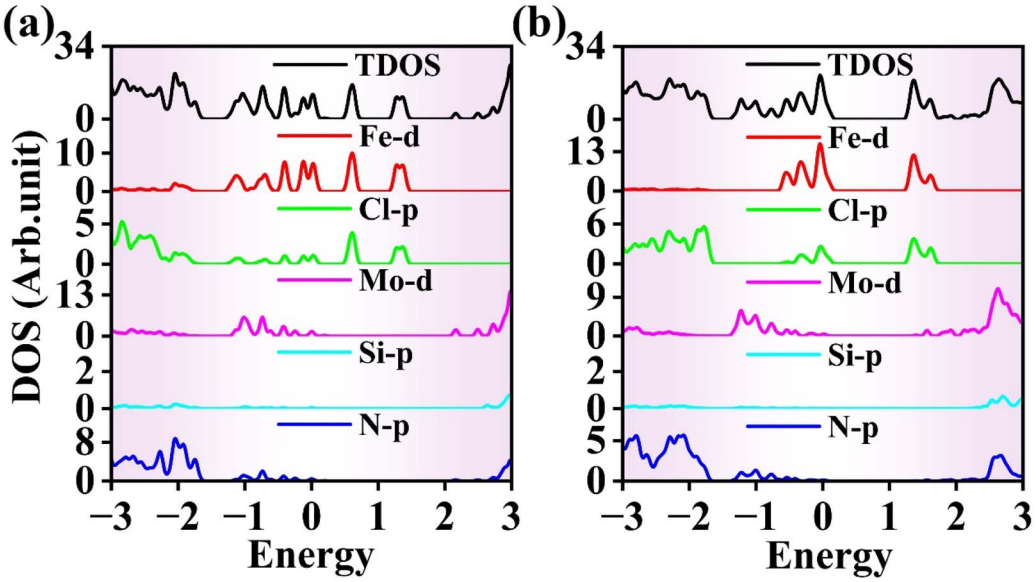

Fig. 10 DOS of $FeCl_3/MoSi_2N_4$ vdWH under in-plane strain of (a) −2 and (b) 0%.

However, in experimental settings, uniaxial strain is typically more feasible for 2D materials. Consequently, we undertook complementary scrutiny of uniaxial strain effects to achieve a comprehensive understanding of strain engineering in the $FeCl_3/MoSi_2N_4$ vdWH. Uniaxial strain analysis is provided in the ESI† to enable a more effective comparative evaluation. Fig. S3(a)† illustrates the direction of the uniaxial strain applied to the $FeCl_3/MoSi_2N_4$ vdWH along the horizontal axis. Fig. S3(b)† illustrates the correlation between the applied uniaxial strain and the band gap. Fig. S3(c)† shows the DOS at $\varepsilon = 3\%$, at which the $FeCl_3/MoSi_2N_4$ vdWH exhibits a type-II band alignment. Additionally, Fig. S3(d)† shows the DOS at $\varepsilon = 4\%$, at which the $FeCl_3/MoSi_2N_4$ vdWH exhibits a type-I band alignment.

3.7 Relationship between applied electric field and electronic structure

The electronic structure and efficacy of semiconductor heterojunctions under an electric field are essential to their practical application. Fig. 11(a) presents a schematic depiction of an electric field applied perpendicular to the $FeCl_3/MoSi_2N_4$ vdWH. The positive direction of the electric field is defined as the one from the $MoSi_2N_4$ monolayer to the $FeCl_3$ monolayer.

Fig. 11(b) shows the relationship between the band gap and the applied electric field. As the electric field strength is increased from −0.7 to 0.8 V Å^{-1}, there is no significant change in the band gap, which fluctuates around 0.9 eV. This indicates that for the $FeCl_3/MoSi_2N_4$ vdWH, the applied electric field does result in any noticeable changes in its band gap. However, when the electric field strength reaches −0.8 V Å^{-1}, the band gap decreases sharply from 0.83 to 0 eV. The modulation of the band gap of the heterojunction and the semiconductor-to-metal transition under an applied vertical electric field can be explained as follows: when a co-directional positive electric field is applied, electron transfer from $FeCl_3$ to $MoSi_2N_4$ is enhanced. However, minimal band gap modulation is observed due to charge transfer saturation and nonlinear band response. Conversely, under a reverse-biased negative field, the strong electric field reverses the net field direction, driving gradual electron transfer from $MoSi_2N_4$ to $FeCl_3$. This progressive accumulation of reverse charges reconstructs interfacial band bending, leading to a gradual narrowing of the band gap. The electric field induces interfacial band bending by creating an electrostatic potential gradient between the $FeCl_3$ and $MoSi_2N_4$ layers. This drives electron redistribution, shifting the Fermi level and altering band alignment. At a critical field strength (*e.g.*, −0.8 V Å^{-1}), the intensified band bending causes the CBM and VBM to overlap in momentum space, effectively closing the band gap, at which point the band gap drops to 0 eV, achieving the transition from a semiconductor to a metal. Simultaneously, charge transfer from low-work-function $MoSi_2N_4$ (5.16 eV) to high-work-function $FeCl_3$ (6.23 eV) generates interfacial dipole moments, further amplifying band realignment. When the electric field exceeds the critical threshold, the Fermi level

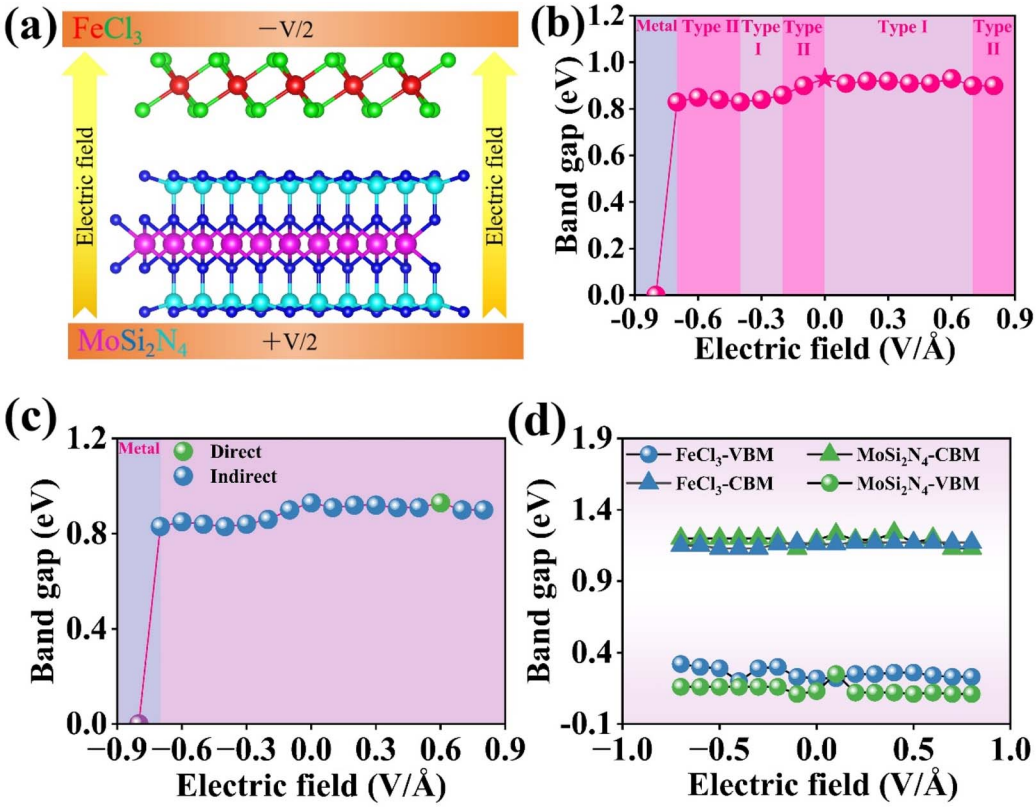

Fig. 11 (a) Schematic of applying an electric field along the *z* direction of vdWH. (b) Band gap of $FeCl_3/MoSi_2N_4$ vdWH as a function of electric field. (c) Band gap nature and (d) shifts in band-edge alignment under an electric field for $FeCl_3/MoSi_2N_4$ vdWH.

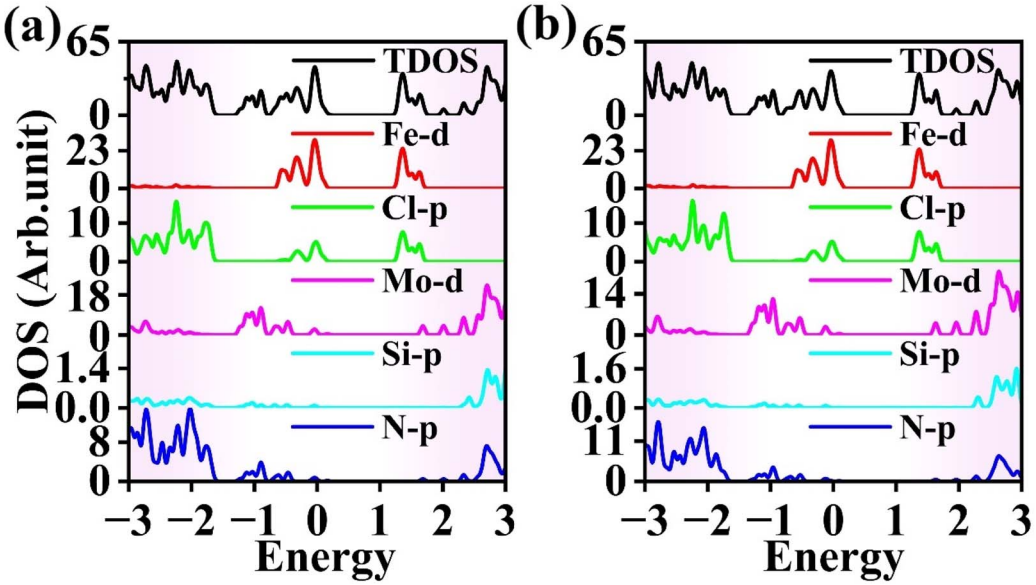

Fig. 12 DOS of the $FeCl_3/MoSi_2N_4$ vdWH when the strength of electric field is (a) −0.2 and (b) 0.2 V Å^{-1}.

penetrates the conduction band, enabling unrestricted electron movement and metallic behavior. This electric-field-tunable electronic transition demonstrates the potential of the heterostructure for reconfigurable nanoelectronic devices.

Fig. 11(c) demonstrates the reversible indirect-to-direct band gap evolution in the heterostructure under an electric field. At an applied electric field strength of 0.6 V Å^{-1}, the VBM and CBM of the heterostructure converge at an identical high-symmetry point within the Brillouin zone, resulting in a direct band gap configuration. Under the other investigated electric field strengths, the heterostructure maintains an indirect band gap nature.

To clarify the mechanism of the band gap tuning using electric fields, we investigated the variation of the band edges in the $FeCl_3/MoSi_2N_4$ vdWH under different electric field strengths, as depicted in Fig. 11(d). Under positive electric fields, the VBM and CBM bands of both $FeCl_3$ and $MoSi_2N_4$ maintain rigid alignment with negligible band gap variation, indicating cooperative stabilization with the built-in electric field. Conversely, under negative electric fields, solely the VBM of $FeCl_3$ undergoes progressive energetic upshifting, while all other band edges (*i.e.*, the CBM of $FeCl_3$, and VBM/CBM of $MoSi_2N_4$) remain largely unchanged. This results in significant band gap narrowing, primarily driven by the elevation of valence band $FeCl_3$. This phenomenon reveals the targeted modulation capability of negative fields on the valence band $FeCl_3$.

Fig. 12(a) presents the DOS at $E = -0.2$ V Å^{-1}. From the figure, it can be seen that the VBE is provided by the Mo 4d orbitals in the $MoSi_2N_4$ monolayer, while the Fe 3d orbitals in the $FeCl_3$ monolayer contribute the CBE. Therefore, the $FeCl_3/MoSi_2N_4$ vdWH exhibits a type-II band alignment. Fig. 12(b) shows the DOS at $E = 0.2$ V Å^{-1}, in which both the VBM and CBM are provided by the Fe 3d orbitals in the $FeCl_3$ monolayer, indicating that the $FeCl_3/MoSi_2N_4$ vdWH has a type-I band alignment. Using a similar analytical method, it can be determined that the $FeCl_3/MoSi_2N_4$ vdWH transitions from type-I to type-II heterojunctions at $E = -0.7$, -0.6, -0.5, -0.2, -0.1, 0.7 and 0.8 V Å^{-1}.

4. Conclusion

This study employed first-principles calculations to investigate the changes in the electronic properties of the $FeCl_3/MoSi_2N_4$ vdWH with modulation of the interlayer distance, in-plane strain, and external electric field. The calculated binding energy, phonon spectra, and molecular dynamics simulations collectively demonstrate robust structural stability. The results indicate that the equilibrium interlayer distance for the $FeCl_3/MoSi_2N_4$ vdWH is 3.35 Å. The band gap of $FeCl_3/MoSi_2N_4$ is 1.21/2.21 eV, as determined using PBE/HSE06 calculations, and both the CBM and VBM are provided by the $FeCl_3$ monolayer, suggesting that it can be classified as a type-I heterojunction. In addition, the VBE is primarily sourced from the Fe 3d states, and the CBE mainly originates from the hybridization between the Fe 3d and Cl 3p orbitals. The work functions of the $FeCl_3$ and $MoSi_2N_4$ monolayers are 6.23 eV and 5.16 eV, respectively, and the work function of the $FeCl_3/MoSi_2N_4$ vdWH is 6.08 eV. The band gap of the $FeCl_3/MoSi_2N_4$ vdWH can be altered by adjusting the interlayer distance, in-plane strain, and applied electric field. The results reveal that the $FeCl_3/MoSi_2N_4$ vdWH not only transitions from a type-I to type-II heterojunction but also shifts from a semiconductor to a metal. As the interlayer distance changes, the band gap decreases. In particular, at $\Delta D =$ 1.5 Å, the band gap becomes zero, indicating a successful transition from semiconductor to metal. When $\Delta D = 2.65$ Å and 5.0 Å, the heterojunction type shifts from type-I to type-II. Within the applied strain ranges from −4 to 4%, the band gap gradually decreases. At $\varepsilon = -4\%$, the band gap is reduced to zero. At strains of −1% and 2%, the heterojunction converts from type-I to type-II. When the applied electric field is in the

range of −0.7 to 0.8 V Å^{-1}, the changes in the band gap are negligible, with the gap remaining around 0.9 eV. However, at E = −0.8 V Å^{-1}, the band gap drops to zero, causing the $FeCl_3$/$MoSi_2N_4$ vdWH to transform into a metal. Therefore, simple adjustment of the interlayer distance, application of strain, and the use of external electric fields can effectively control the band gap and band alignment type of $FeCl_3$/$MoSi_2N_4$ vdWH. These characteristics suggest the tunability and excellent electronic properties of the $FeCl_3$/$MoSi_2N_4$ vdWH, indicating its broad application prospects in photodetectors, wearable devices, flexible electronics and optoelectronic devices.

Data availability

The datasets used and analysed during the current study are available from the corresponding author upon reasonable request.

Author contributions

Xinrui Chen: original draft writing, data curation. Su Su: data curation, investigation. Xuewen Wang: data curation, methodology. Xuanyu Chen: data curation, investigation. Syed Awais Ahmad: writing, methodology, investigation. Lin Xu: supervision, data curation, investigation, writing. Weibin Zhang: supervision, data curation, investigation, writing.

Conflicts of interest

The authors declare that they have no known competing financial interests or personal relationships that could have influenced the work reported in this paper.

Acknowledgements

This research was supported by the National Natural Science Foundation of China (No. 52262042) and Yunnan Fundamental Research Projects (grant No. 202301AT070060). Spring City Plan: the High-level Talent Promotion and Training Project of Kunming (2022SCP005), Yunnan Revitalization Talent Support Program.

References

1 T. M. Su and X. W. Zhu, Advanced Photocatalytic Materials for Environmental and Energy Applications, *Materials*, 2023, **16**, 7197, DOI: 10.3390/ma16227197.
2 M. Ramírez-Hernández, J. Cox, B. Thomas and T. Asefa, Nanomaterials for Removal of Phenolic Derivatives from Water Systems: Progress and Future Outlooks, *Molecules*, 2023, **28**, 6568, DOI: 10.3390/molecules28186568.
3 K. S. Novoselov, A. K. Geim, S. V. Morozov, D. Jiang, Y. Zhang, S. V. Dubonos, I. V. Grigorieva and A. A. Firsov, Electric field effect in atomically thin carbon films, *Science*, 2004, **306**, 666–669, DOI: 10.1126/science.1102896.
4 K. S. Novoselov, A. K. Geim, S. V. Morozov, D. Jiang, M. I. Katsnelson, I. V. Grigorieva, S. V. Dubonos and A. A. Firsov, Two-dimensional gas of massless Dirac fermions in graphene, *Nature*, 2005, **438**, 197–200, DOI: 10.1038/nature04233.
5 D. B. Farmer, H.-Y. Chiu, Y.-M. Lin, K. A. Jenkins, F. Xia and P. Avouris, Utilization of a Buffered Dielectric to Achieve High Field-Effect Carrier Mobility in Graphene Transistors, *Nano Lett.*, 2009, **9**, 4474–4478, DOI: 10.1021/nl902788u.
6 P. Boggild, Research on scalable graphene faces a reproducibility gap, *Nat. Commun.*, 2023, **14**, 7495, DOI: 10.1038/s41467-023-36891-5.
7 M. M. Uddin, M. H. Kabir, M. A. Ali, M. M. Hossain, M. U. Khandaker, S. Mandal, A. Arifutzzaman and D. Jana, Graphene-like emerging 2D materials: recent progress, challenges and future outlook, *RSC Adv.*, 2023, **13**, 33336–33375, DOI: 10.1039/d3ra04456d.
8 W. Zhang, Z. Zhang, S. Kwon, F. Zhang, B. Stephen, K. K. Kim, R. Jung, S. Kwon, K.-B. Chung and W. Yang, Photocatalytic improvement of Mn-adsorbed g-C_3N_4, *Appl. Catal., B*, 2017, **206**, 271–281, DOI: 10.1016/j.apcatb.2017.01.034.
9 X. C. Ma, X. Wu, H. D. Wang and Y. C. Wang, A Janus MoSSe monolayer: a potential wide solar-spectrum water-splitting photocatalyst with a low carrier recombination rate, *J. Mater. Chem. A*, 2018, **6**, 2295–2301, DOI: 10.1039/c7ta10015a.
10 L. Xu, W. Q. Huang, L. L. Wang, Z. A. Tian, W. Y. Hu, Y. M. Ma, X. Wang, A. L. Pan and G. F. Huang, Insights into Enhanced Visible-Light Photocatalytic Hydrogen Evolution of g-C_3N_4 and Highly Reduced Graphene Oxide Composite: The Role of Oxygen, *Chem. Mater.*, 2015, **27**, 1612–1621, DOI: 10.1021/cm504265w.
11 M. D. Hernandez-Alonso, F. Fresno, S. Suarez and J. M. Coronado, Development of alternative photocatalysts to TiO_2: Challenges and opportunities, *Energy Environ. Sci.*, 2009, **2**, 1231–1257, DOI: 10.1039/b907933e.
12 S. Huang, D. Luo, B. Yang, G. Chen, X. Liu, Z. Mei and N. Zhang, Constructing highly active interface between layered $Ni(OH)_2$ and porous Mo_2N for efficient electrocatalytic oxygen evolution reaction, *Int. J. Hydrogen Energy*, 2023, **48**, 22091–22100, DOI: 10.1016/j.ijhydene.2023.03.121.
13 K. Qi, C. Zhuang, M. Zhang, P. Gholami and A. Khataee, Sonochemical synthesis of photocatalysts and their applications, *J. Mater. Sci. Technol.*, 2022, **123**, 243–256, DOI: 10.1016/j.jmst.2022.02.019.
14 R. Marschall, Semiconductor Composites: Strategies for Enhancing Charge Carrier Separation to Improve Photocatalytic Activity, *Adv. Funct. Mater.*, 2014, **24**, 2421–2440, DOI: 10.1002/adfm.201303214.
15 Q. Cui, X. Gu, Y. Zhao, K. Qi and Y. Yan, S-scheme $CuInS_2$/ZnS heterojunctions for the visible light-driven photocatalytic degradation of tetracycline antibiotic drugs, *J. Taiwan Inst. Chem. Eng.*, 2023, **142**, 104679, DOI: 10.1016/j.jtice.2023.104679.
16 J. Zhang, Y. Zhao, K. Qi and S.-y. Liu, $CuInS_2$ quantum-dot-modified g-C_3N_4 S-scheme heterojunction photocatalyst for hydrogen production and tetracycline degradation, *J.*

Mater. Sci. Technol., 2024, **172**, 145–155, DOI: 10.1016/j.jmst.2023.06.042.

17 J. Lee and G. Kim, Electronic properties of a graphene/periodic porous graphene heterostructure, *Carbon*, 2017, **122**, 281–286, DOI: 10.1016/j.carbon.2017.06.049.

18 K. Ren, K. Wang, Y. Cheng, W. Tang and G. Zhang, Two-dimensional heterostructures for photocatalytic water splitting: a review of recent progress, *Nano Futures*, 2020, **4**, 032006, DOI: 10.1088/2399-1984/abacab.

19 W. Zhang, J. Guo, X. Lv and F. Zhang, Combined Machine Learning and High-Throughput Calculations Predict Heyd–Scuseria–Ernzerhof Band Gap of 2D Materials and Potential $MoSi_2N_4$ Heterostructures, *J. Phys. Chem. Lett.*, 2024, **15**, 5413–5419, DOI: 10.1021/acs.jpclett.4c01013.

20 A. Castro-Carranza, J. C. Nolasco, S. Bley, M. Rückmann, F. Meierhofer, L. Mädler, T. Voss and J. Gutowski, Effects of $FeCl_3$ as Oxidizing Agent on the Conduction Mechanisms in Polypyrrole (PPy)/pc-ZnO Hybrid Heterojunctions Grown by Oxidative Chemical Vapor Deposition, *J. Polym. Sci. Part B: Polym. Phys.*, 2016, **54**, 1537–1544, DOI: 10.1002/polb.24049.

21 D. Zhan, J. X. Yan, Z. H. Ni, L. Sun, L. F. Lai, L. Liu, X. Y. Liu and Z. X. Shen, Bandgap-Opened Bilayer Graphene Approached by Asymmetrical Intercalation of Trilayer Graphene, *Small*, 2015, **11**, 1177–1182, DOI: 10.1002/smll.201402728.

22 D. Zhan, L. Sun, Z. H. Ni, L. Liu, X. F. Fan, Y. Y. Wang, T. Yu, Y. M. Lam, W. Huang and Z. X. Shen, $FeCl_3$-Based Few-Layer Graphene Intercalation Compounds: Single Linear Dispersion Electronic Band Structure and Strong Charge Transfer Doping, *Adv. Funct. Mater.*, 2010, **20**, 3504–3509, DOI: 10.1002/adfm.201000641.

23 X.-G. Hu, Q. Wei, Y.-M. Zhao, P.-X. Hou, W. Ren, C. Liu and H.-M. Cheng, $FeCl_3$-functionalized graphene oxide/single-wall carbon nanotube/silicon heterojunction solar cells with an efficiency of 17.5%, *J. Mater. Chem. A*, 2022, **10**, 4644–4652, DOI: 10.1039/d2ta00217e.

24 A. Bafekry, M. Faraji, A. A. Ziabari, M. M. Fadlallah, C. V. Nguyen, M. Ghergherehchi and S. A. H. Feghhi, A van der Waals heterostructure of $MoS_2/MoSi_2N_4$: a first-principles study, *New J. Chem.*, 2021, **45**, 8291–8296, DOI: 10.1039/d1nj00344e.

25 J. Zeng, L. Xu, Y. Yang, X. Luo, H.-J. Li, S. X. Xiong and L.-L. Wang, Boosting the photocatalytic hydrogen evolution performance of monolayer C_2N coupled with $MoSi_2N_4$: density-functional theory calculations, *Phys. Chem. Chem. Phys.*, 2021, **23**, 8318–8325, DOI: 10.1039/d1cp00364j.

26 D. K. Pham, Electronic properties of a two-dimensional van der Waals $MoGe_2N_4/MoSi_2N_4$ heterobilayer: effect of the insertion of a graphene layer and interlayer coupling, *RSC Adv.*, 2021, **11**, 28659–28666, DOI: 10.1039/d1ra04531h.

27 Q. Li, W. Zhou, X. Wan and J. Zhou, Strain effects on monolayer $MoSi_2N_4$: Ideal strength and failure mechanism, *Phys. E*, 2021, **131**, 114753, DOI: 10.1016/j.physe.2021.114753.

28 G. K. Yang and Y. A. Zhou, $MoSi_2N_4/WO_2$ van der Waals heterostructure: Theoretical prediction of an effective strategy to boost $MoSi_2N_4$'s nanoelectronic and optoelectronic applications, *Comput. Mater. Sci.*, 2024, **231**, 112617, DOI: 10.1016/j.commatsci.2023.112617.

29 X. Cai, Z. Zhang, Y. Zhu, L. Lin, W. Yu, Q. Wang, X. Yang, X. Jia and Y. Jia, A two-dimensional $MoSe_2/MoSi_2N_4$ van der Waals heterostructure with high carrier mobility and diversified regulation of its electronic properties, *J. Mater. Chem. C*, 2021, **9**, 10073–10083, DOI: 10.1039/d1tc01149a.

30 J. Q. Ng, Q. Wu, L. K. Ang and Y. S. Ang, Tunable electronic properties and band alignments of $MoSi_2N_4$/GaN and $MoSi_2N_4$/ZnO van der Waals heterostructures, *Appl. Phys. Lett.*, 2022, **120**, 103101, DOI: 10.1063/5.0083736.

31 G. Kresse and J. Furthmüller, Efficiency of *ab initio* total energy calculations for metals and semiconductors using a plane-wave basis set, *Comput. Mater. Sci.*, 1996, **6**, 15–50, DOI: 10.1016/0927-0256(96)00008-0.

32 S. Grimme, Semiempirical GGA-type density functional constructed with a long-range dispersion correction, *J. Comput. Chem.*, 2006, **27**, 1787–1799, DOI: 10.1002/jcc.20495.

33 J. Heyd, G. E. Scuseria and M. Ernzerhof, Hybrid functionals based on a screened Coulomb potential, *J. Chem. Phys.*, 2003, **118**, 8207–8215, DOI: 10.1063/1.1564060.

34 C. Q. Nguyen, Y. S. Ang, S.-T. Nguyen, N. V. Hoang, N. M. Hung and C. V. Nguyen, Tunable type-II band alignment and electronic structure of $C_3N_4/MoSi_2N_4$ heterostructure: Interlayer coupling and electric field, *Phys. Rev. B*, 2022, **105**, 045303, DOI: 10.1103/PhysRevB.105.045303.

35 Y.-L. Hong, Z. Liu, L. Wang, T. Zhou, W. Ma, C. Xu, S. Feng, L. Chen, M.-L. Chen, D.-M. Sun, X.-Q. Chen, H.-M. Cheng and W. Ren, Chemical vapor deposition of layered two-dimensional $MoSi_2N_4$ materials, *Science*, 2020, **369**, 670, DOI: 10.1126/science.abb7023.

36 Y. Guo, L. Zhao and D. Zheng, Theoretical investigation on the electronic structure of new InSe/CrS_2 van der Waals heterostructure, *J. Mater. Res.*, 2022, **37**, 2157–2164, DOI: 10.1557/s43578-022-00548-8.

37 M. K. Mohanta and A. De Sarkar, Interfacial hybridization of Janus MoSSe and BX (X = P, As) monolayers for ultrathin excitonic solar cells, nanopiezotronics and low-power memory devices, *Nanoscale*, 2020, **12**, 22645–22657, DOI: 10.1039/d0nr07000a.

38 D. Singh, N. Khossossi, A. Ainane and R. Ahuja, Modulation of 2D GaS/BTe vdW heterostructure as an efficient HER catalyst under external electric field influence, *Catal. Today*, 2021, **370**, 14–25, DOI: 10.1016/j.cattod.2020.09.025.

39 M. Yankowitz, K. Watanabe, T. Taniguchi, P. San-Jose and B. J. LeRoy, Pressure-induced commensurate stacking of graphene on boron nitride, *Nat. Commun.*, 2016, **7**, 13168, DOI: 10.1038/ncomms13168.

40 Z. Dai, L. Bai, J. Wang and Z. Zhang, A first-principles study of $Ti_2B_2T_2/MoSi_2N_4$ (T = F, O, OH) van der Waals heterostructures: Response characteristics to external electric field and uniaxial strain, *Surf. Interfaces*, 2024, **48**, 104305, DOI: 10.1016/j.surfin.2024.104305.